Supporting information

Simultaneous Sulfide Remediation and Low-Voltage Hydrogen Production Enabled by Ru-Doped CoNi Sulfide Catalysts

Zhiqiang Peng, Hao Zhou, Kun Wang, Zhang-Hui Lu**

Key Laboratory of Green Catalysis of Jiangxi Education Institutes, Key Laboratory of Green Hydrogen and Advanced Catalysis of Jiangxi Province, Key Laboratory of Fluorine and Silicon for Energy Materials and Chemistry of Ministry of Education College of Chemistry and Materials, Jiangxi Normal University, Nanchang 330022, China

**E-mail: luzh@jxnu.edu.cn (Zhang-Hui Lu);kunwang@jxnu.edu.cn (Kun Wang)*

Experimental section

Chemicals

Shanghai Aladdin Biochemical Technology Co., Ltd. (China) supplied the following reagents: sodium hydroxide (NaOH, ⩾98%), cobalt(II) nitrate hexahydrate ($Co(NO_3)_2 \cdot 6H_2O$, 99%), urea ($CO(NH_2)_2$, 99.5%), ammonium fluoride (NH_4F, 98%), sodium sulfide nonahydrate ($Na_2S \cdot 9H_2O$, ⩾98%), and ruthenium(III) chloride hydrate ($RuCl_3 \cdot xH_2O$, 35.0-42.0% Ru basis). Both hydrochloric acid (HCl) and sulfuric acid (H_2SO_4) were purchased from Sinopharm Chemical Reagent Co., Ltd. Nickel foam (NF, 1.5 mm thick) was purchased from Kunshan Lvchuang Technology Co., Ltd. Ultrapure water used in all experiments was obtained from a Millipore system.

Materials characterization

Crystallographic analysis was performed using an X-ray diffractometer (XRD, Bruker D8 ADVANCE) with Cu Kα radiation (λ = 1.5406 Å) at 40 kV accelerating voltage and 40 mA applied current. Morphological features were characterized using field-emission scanning electron microscopy (FE-SEM, TESCAN CLARA) and transmission electron microscopy (TEM, FEI Talos F200x). To investigate the surface electronic structure, X-ray photoelectron spectroscopy (XPS) was performed using a Thermo Scientific K-Alpha spectrometer (Al Kα excitation). Brunauer-Emmett-Teller (BET) specific surface areas were obtained from nitrogen physisorption measurements using a Quantachrome Autosorb IQ analyzer. An Agilent 5110 system (ICP-OES) was utilized to quantify the elemental metal composition. The concentration of dissolved ions was monitored using a Lengguang 759s UV-Vis spectrophotometer (Shanghai). The wettability of molten sulfur on the catalyst surface was evaluated by the sessile drop method using a Krüss DSAHT17C contact-angle analyzer.

Electrochemical measurements

To determine the electrochemically active surface area (ECSA), we assessed the double-layer capacitance (C_{dl}). Cyclic voltammetry (CV) curves were recorded in the non-Faradaic region at scan rates of 20, 30, 40, 50, and 60 mV s^{-1}. The C_{dl} value was derived from the slope of the linear plot of $\Delta j/2$ ($\Delta j = j_a -$

j_c) versus scan rate. Subsequently, the ECSA was calculated by normalizing the C_{dl} with respect to the specific capacitance of a standard planar reference electrode. The ECSA was calculated according to Equ. 1:

$$ECSA = C_{dl}/C_s \quad \text{(Equ. 1)}$$

where C_{dl} and C_s denote the double layer capacitance and specific capacitance, respectively. C_{dl} was derived from CV curves acquired in the non-Faradaic region, and a specific capacitance (C_s) of 0.04 mF cm^{-2} was adopted for the alkaline electrolyte system.

Calculation of the Faradaic efficiency for H_2 evolution

The hydrogen production volume (V_{H2}) was quantified via the water displacement method, with the molar volume (V_m) of hydrogen gas determined to be 24.5 L mol^{-1} at 25 °C and 1 atm. The Faradaic efficiency (FE) for H_2 production was calculated according to Equ. 2 and 3:

$$n_{H_2} = H_2/V_m \quad \text{(Equ. 2)}$$

$$FE_{H2} = n_{H2} \times N \times F/(I \times t) \quad \text{(Equ. 3)}$$

where n_{H2} refers to the molar quantity of produced hydrogen gas, N denotes the electron transfer number (N = 2 for HER), F stands for the Faraday constant (96485 C mol^{-1}), I denotes the applied current, and t represents the total electrolysis time.

UV-vis analysis for sulfion oxidation reaction

The concentrations of S^{2-} and polysulfide ions (S_n^{2-}) during the SOR were quantified using UV-vis spectrophotometry. First, a calibration curve for S^{2-} was established by measuring the absorbance of standard solutions at a wavelength of λ = 230 nm. Similarly, a calibration curve for S_n^{2-} was constructed using reference standards prepared from equimolar mixtures of elemental sulfur and Na_2S. To monitor the reaction, anolyte samples were collected at various intervals during the SOR process (carried out at a current density of 300 mA cm^{-2}). The aliquots used for S^{2-} and S_n^{2-} quantification were diluted by factors of 5000 and 50, respectively, prior to UV-vis analysis. The concentrations of S^{2-} and S_n^{2-} were then determined from the established calibration curves. Reproducibility was verified by performing the electrolysis in 50 mL of solution under identical conditions.

Computational details

Density functional theory as implemented in the Vienna Ab-initio Simulation Package (VASP) was employed to optimize geometry structures.[1,2] The exchange-correlation interactions were described by the generalized gradient approximation (GGA) in the form of the Perdew-Burke-Ernzerhof functional (PBE).[3] We have chosen the projected augmented wave (PAW) potentials[4,5] to describe the ionic cores and take valence electrons into account using a plane wave basis set with a kinetic energy cutoff of 450 eV. The electronic energy was considered self-consistent when the energy change was smaller than 10^{-5} eV. A geometry optimization was considered convergent when the force change was smaller than 0.04 eV/Å. The vacuum spacing in a direction perpendicular to the plane of the structure is 15 Å. The van der Waals interactions were considered by the method of the Grimme (DFT + D3)].[6] The Brillouin-zone integration was sampled with a Monkhorst-Pack mesh of 2 × 2 × 1 in the structural relaxation calculations.

The Gibbs free energy change (ΔG) of a gas phase molecule or an adsorbate on the surface was calculated based on Nørskov's computational hydrogen electrode (CHE) method by the equ. 4:[7]

$$\Delta G = \Delta E + \Delta EZPE - T\Delta S \quad \text{(Equ. 4)}$$

where ΔE is the total energy change directly obtained from DFT calculations, ZPE is the zero-point energy change, ΔS is the entropy correction change, T is the temperature which is normally estimated at 298.15 K.

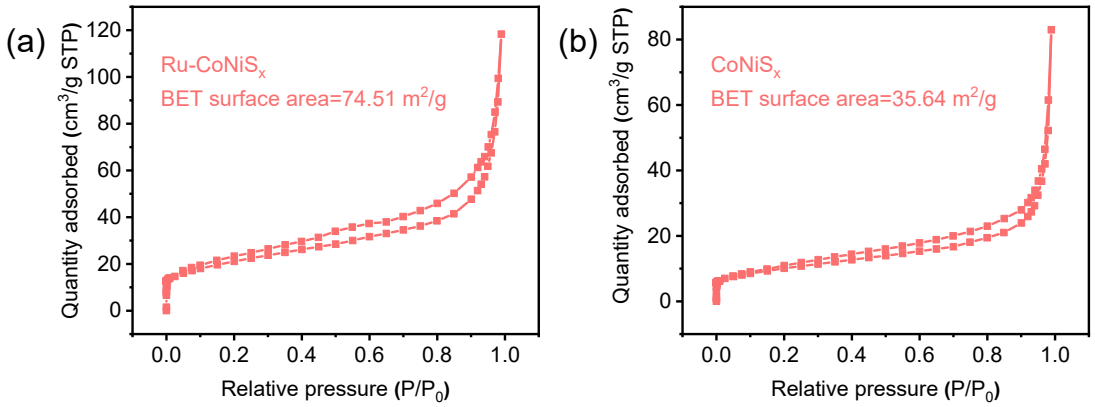

Figure S1. (a) and (b) Nitrogen adsorption-desorption isotherms for Ru-CoNiS$_x$ and CoNiS$_x$ catalysts.

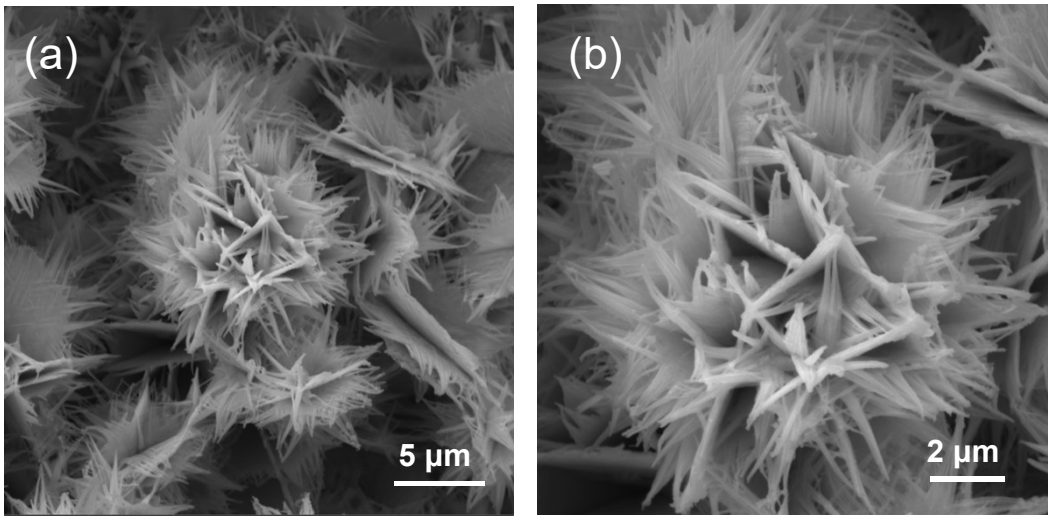

Figure S2. SEM images of $CoNiS_x$/NF.

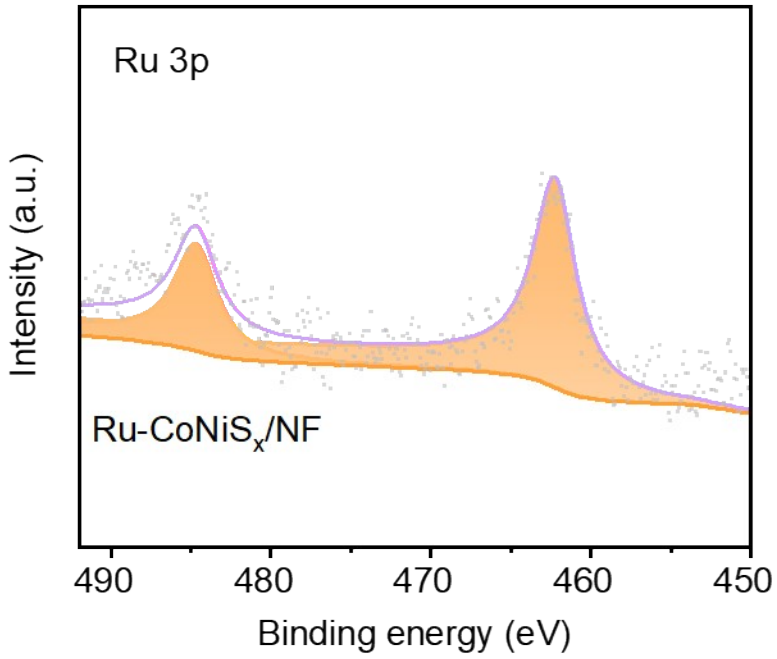

Figure S3. High-resolution spectrum of Ru 3p for Ru-CoNiS$_x$/NF.

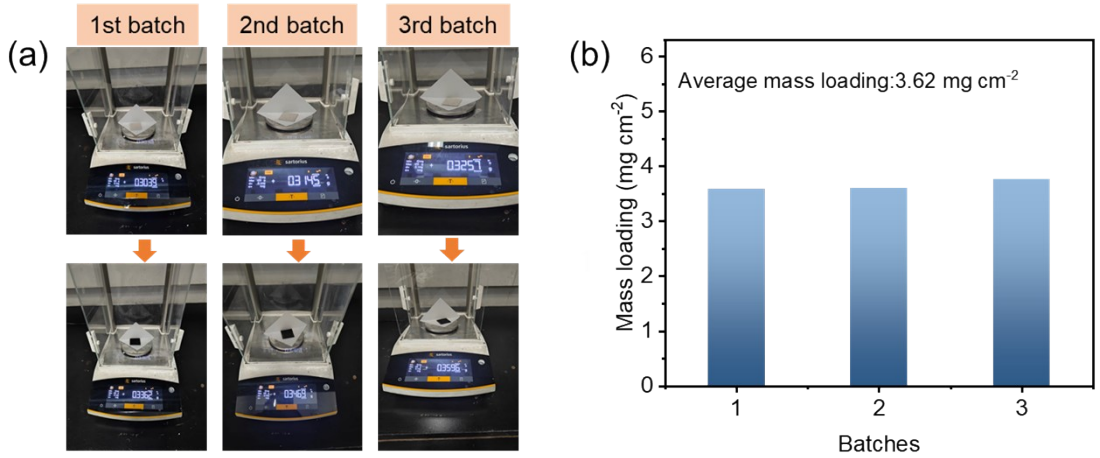

Figure S4. (a) Photographs of three independent weighing measurements before and after the *in-situ* growth of Ru-CoNiS_x on nickel foam. (b) Summarized average mass loading of the Ru-CoNiS_x/NF electrodes calculated from the three batches.

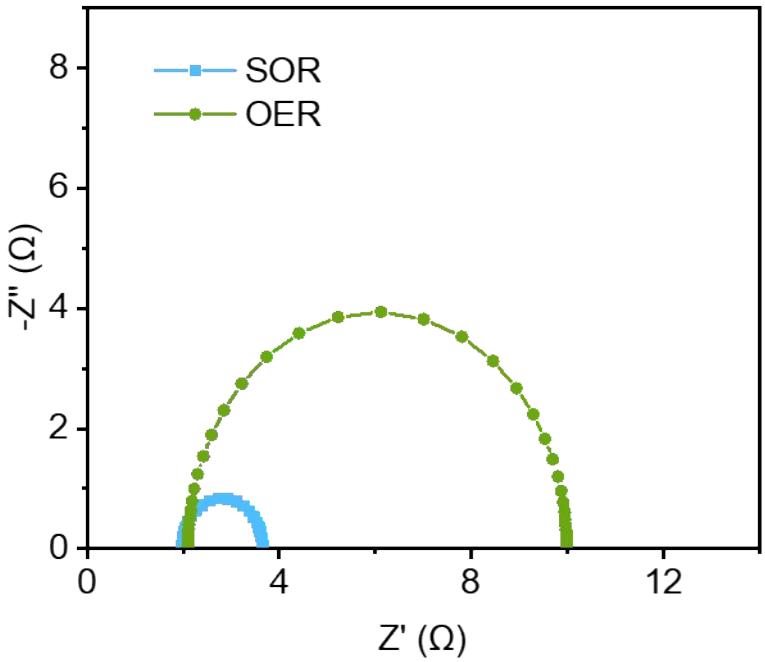

Figure S5. Nyquist plots of Ru-CoNiS$_x$/NF for SOR in 1.0 M NaOH +1.0 M Na_2S and OER in 1.0 M NaOH.

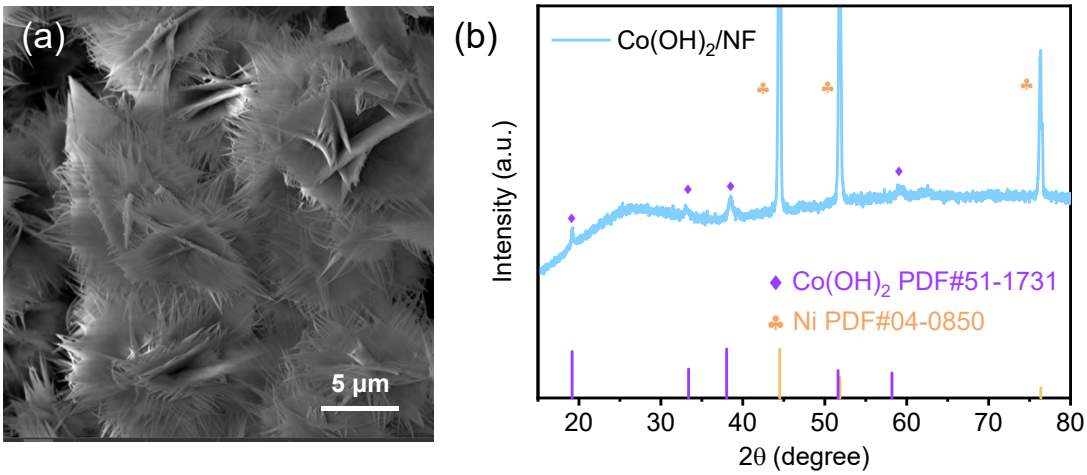

Figure S6. (a) SEM image and (b) XRD patterns of $Co(OH)_2$/NF.

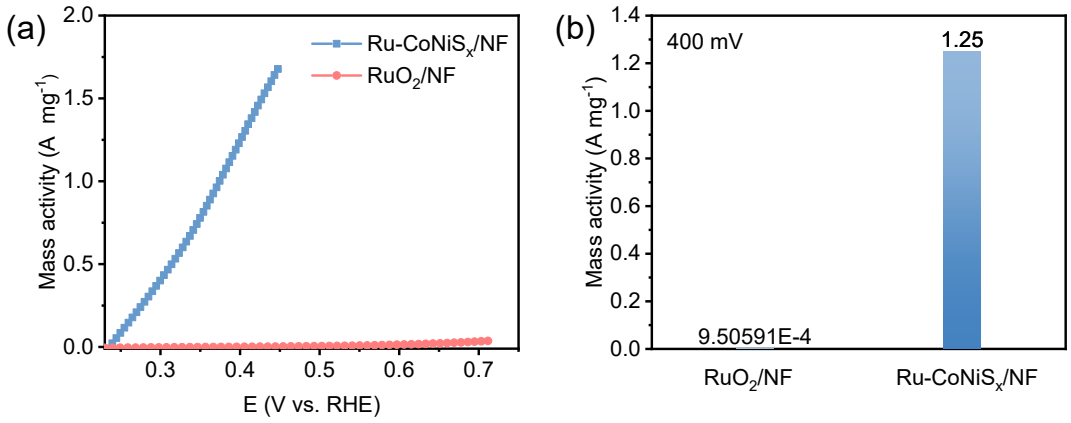

Figure S7. (a) The mass activities of Ru-CoNiS$_x$/NF and RuO$_2$/NF toward the SOR. (b) comparison of mass activities values at 400 mV vs. RHE.

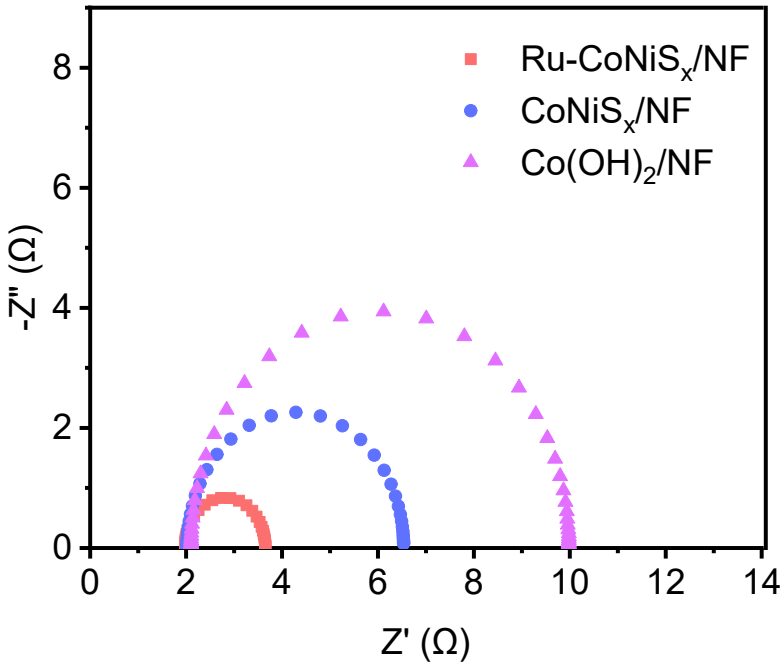

Figure S8. (a) Nyquist plots of Ru-CoNiS$_x$/NF, CoNiS$_x$/NF and Co(OH)$_2$/NF in SOR process.

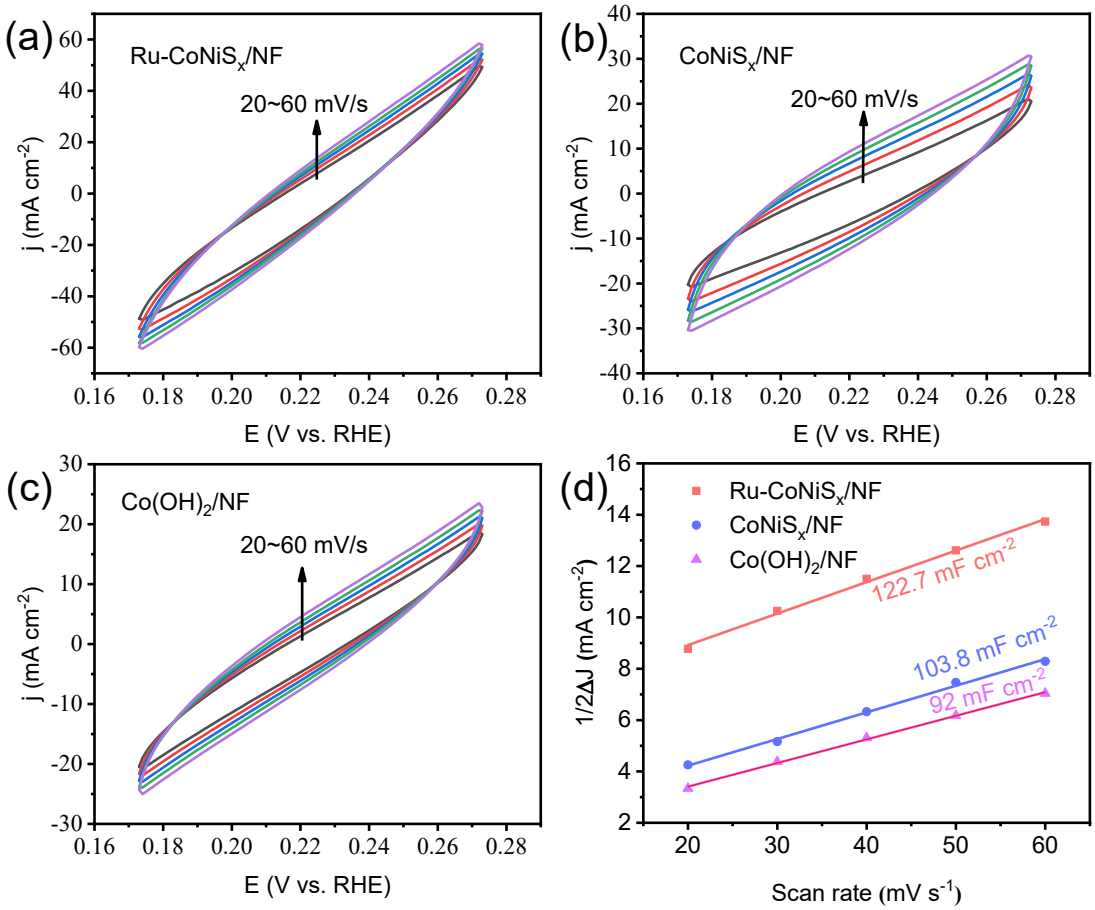

Figure S9. CV curves of (a) Ru-CoNiS$_x$/NF, (b) CoNiS$_x$/NF, (c) Co(OH)$_2$ in 1.0 M Na_2S + 1.0 M NaOH. (d) C_{dl} of different electrocatalysts.

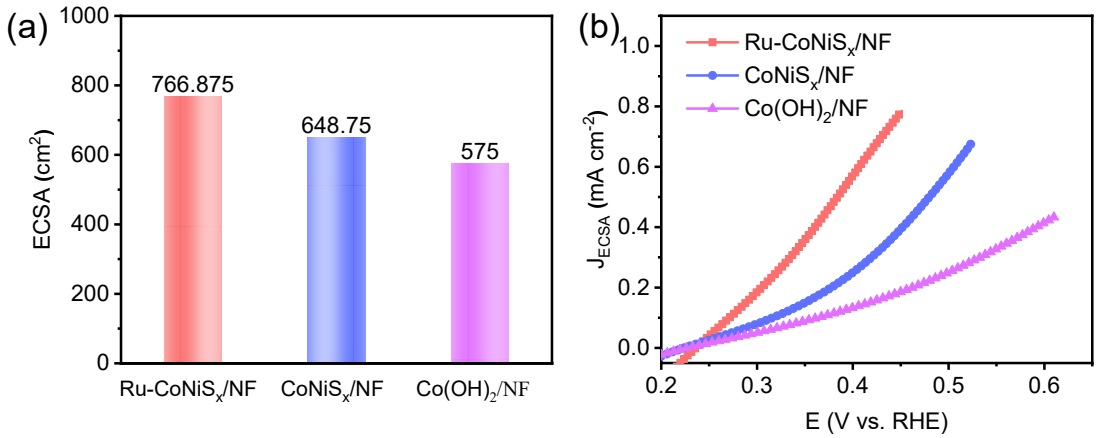

Figure S10. (a) The corresponding evaluated ECSA values (b) SOR polarization curves normalized by ECSA.

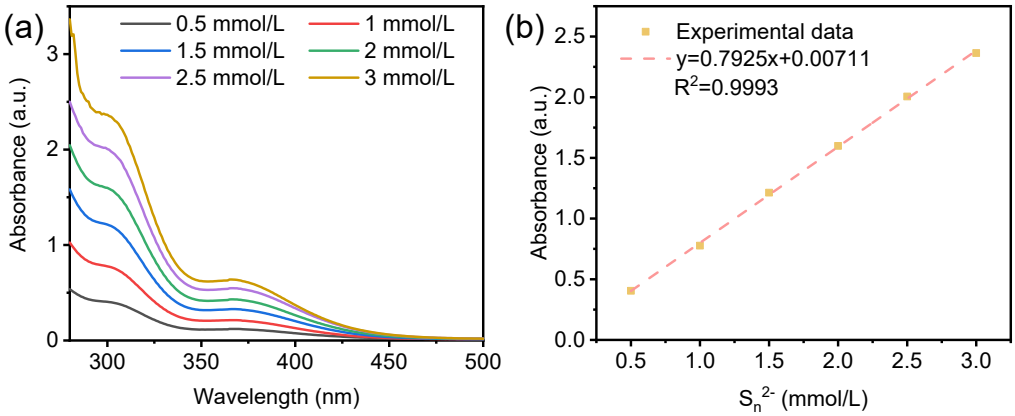

Figure S11. (a) UV–vis absorption spectrum of S_n^{2-} with different concentration and (b) calibration curve.

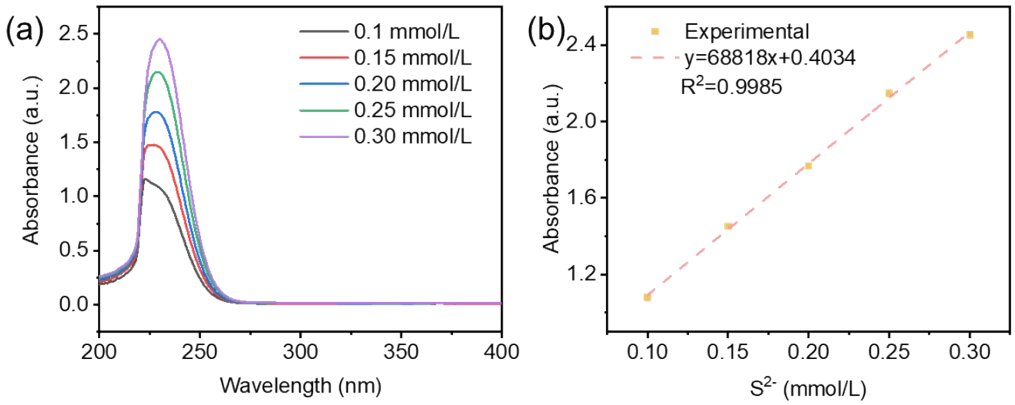

Figure S12. (a) UV-vis absorption spectrum of S^{2-} with different concentration and (b) calibration curve.

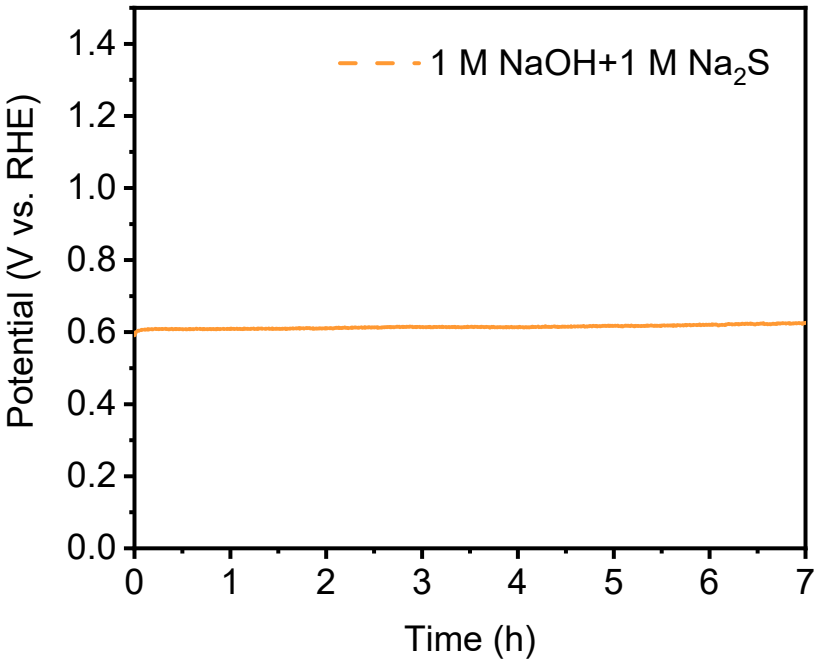

Figure S13. (a) Chronopotentiometry curve of Ru-CoNiS_x/NF during SOR in 7 h test.

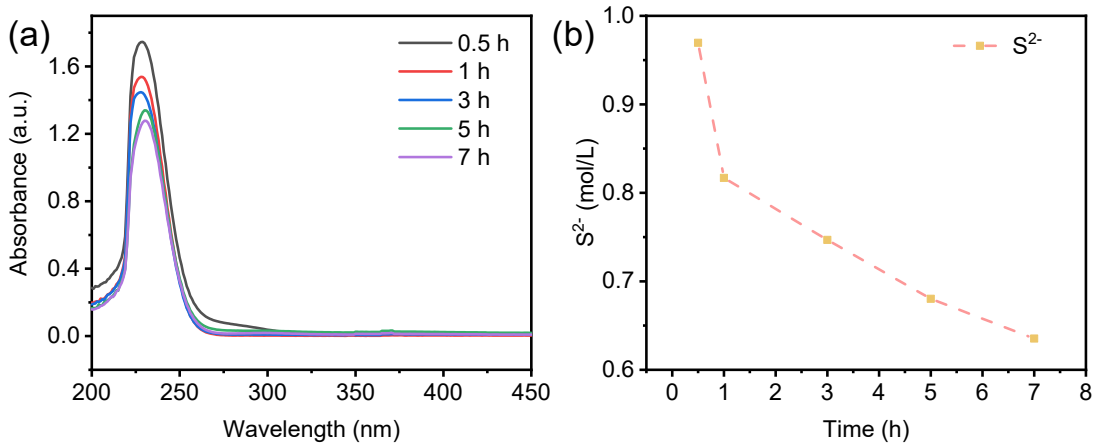

Figure S14. (a) UV-vis spectra of electrolyte during SOR after 5000 times dilution. (b) Sulfion concentrations of electrolyte during SOR before 5000 times dilution.

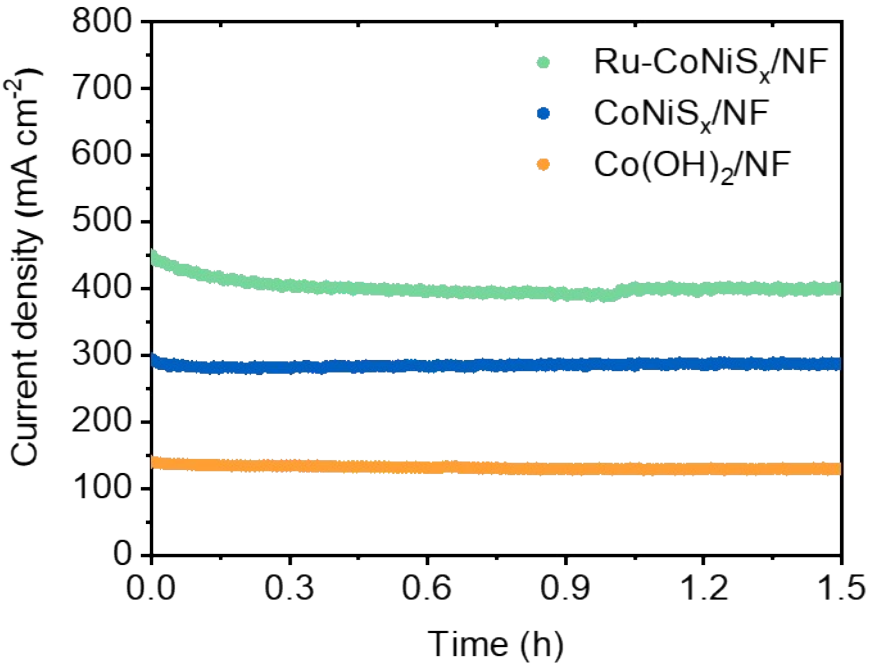

Figure S15. The time-dependent current density curve of different catalysts during SOR in 1.5 h test.

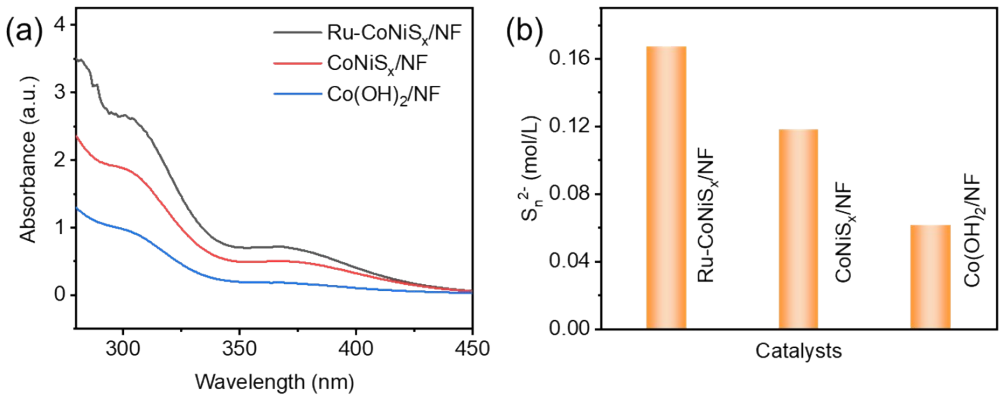

Figure S16. (a) UV-vis absorption spectra of various catalysts for SOR at 0.6 V versus RHE. (b) Comparison of S_n^{2-} production by different catalysts at 0.6 V during SOR.

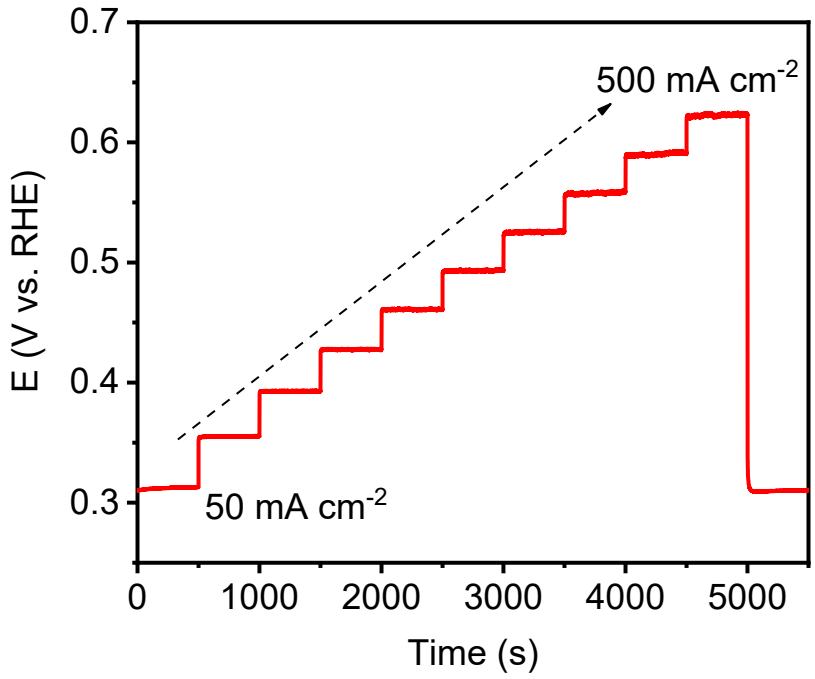

Figure S17. Multi-step chronopotentiometry of the Ru-CoNiS_x/NF catalyst with the current density stepped from 50 to 500 mA cm^{-2}.

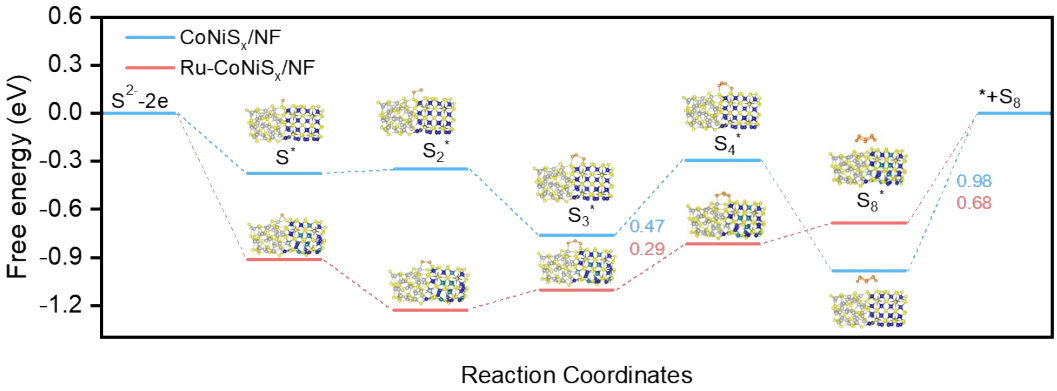

Figure S18. Free-energy diagrams of sulfide oxidation on $CoNiS_x$ and Ru-$CoNiS_x$.

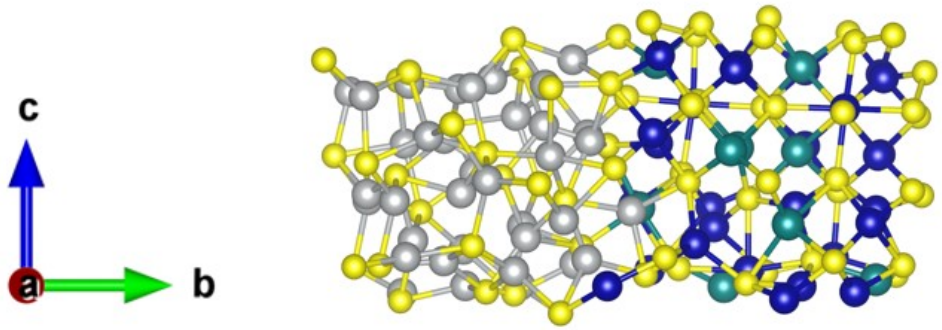

Figure S19. The atomic structure model of Ru-CoNiS_x. The gray, blue, cyan, and yellow spheres refer to the Ni, Co, Ru, and S atoms, respectively.

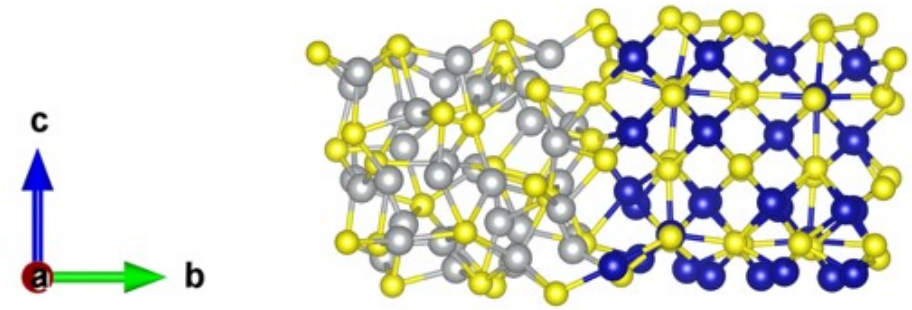

Figure S20. The atomic structure model of $CoNiS_x$. The gray, blue, and yellow spheres refer to the Ni, Co, and S atoms, respectively.

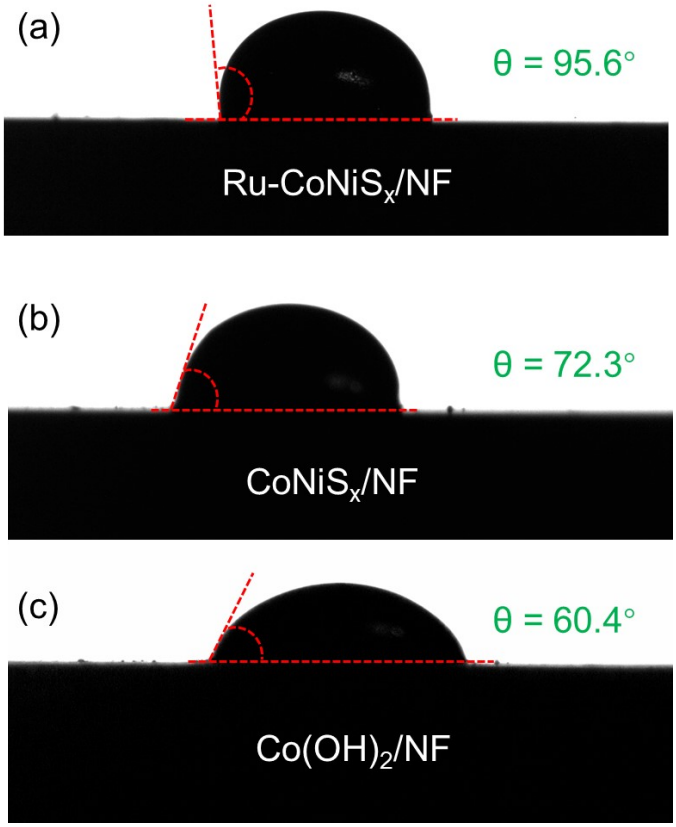

Figure S21. Interfacial Contact Angles of Molten Sulfur Droplets on Various Material Surfaces. (a) Ru-$CoNiS_x$/NF. (b) $CoNiS_x$/NF. (c) $Co(OH)_2$/NF.

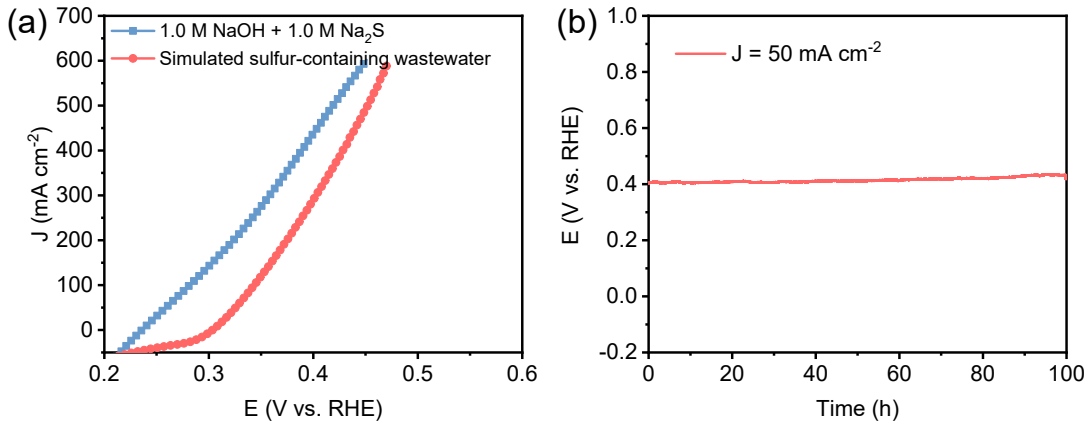

Figure S22. (a) LSV curves of Ru-CoNiS$_x$/NF for the SOR in the base electrolyte (1.0 M NaOH + 1.0 M Na_2S) and simulated sulfide-containing wastewater. (b) Durability test of Ru-CoNiS$_x$/NF for the SOR in simulated sulfide-containing wastewater at 50 mA cm^{-2}.

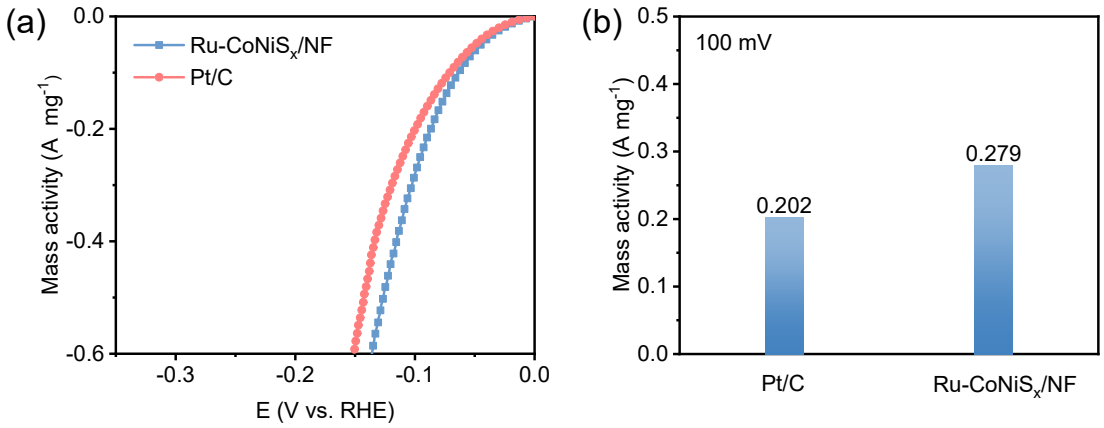

Figure S23. (a) The mass activities of Ru-CoNiS$_x$/NF and Pt/C toward the HER. (b) comparison of mass activities values at a 100 mV overpotential.

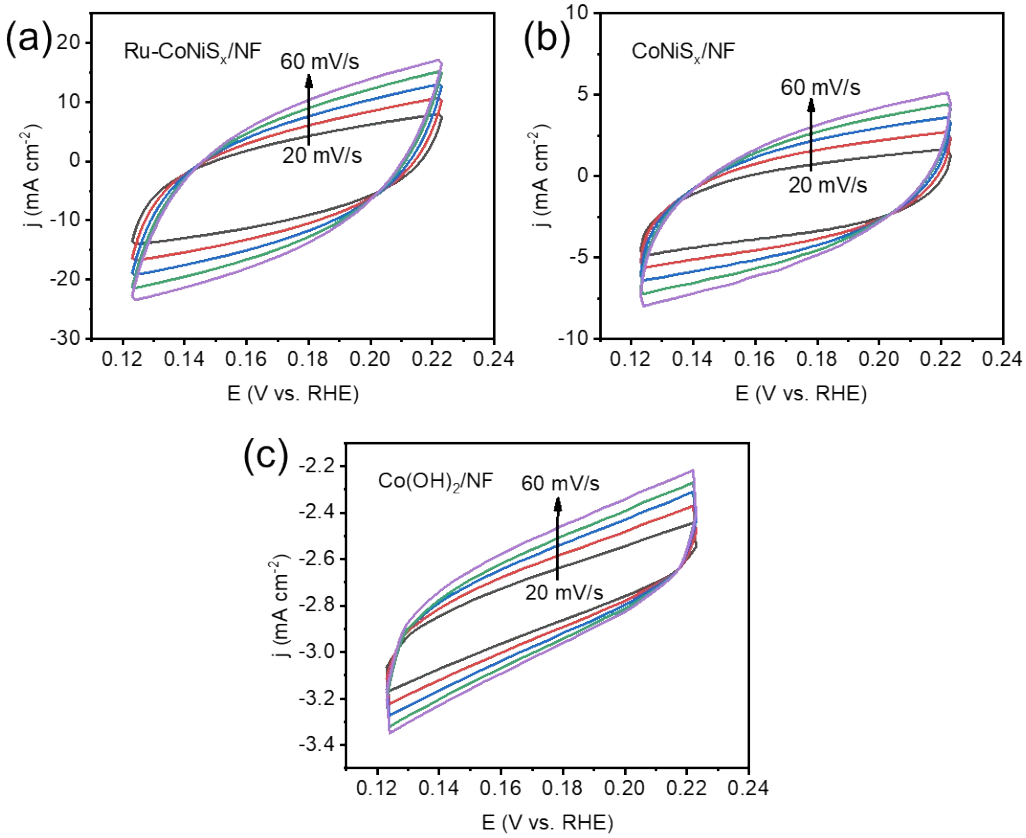

Figure S24. CV curves of (a) Ru-CoNiS$_x$/NF, (b) CoNiS$_x$/NF and (c) Co(OH)$_2$/NF in 1.0 M NaOH.

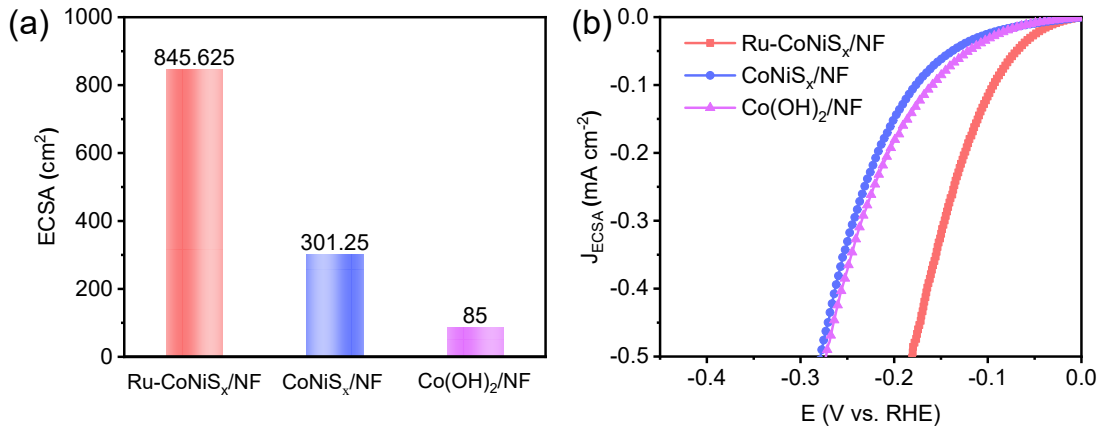

Figure S25. (a)The corresponding evaluated ECSA values (b) HER polarization curves normalized by ECSA.

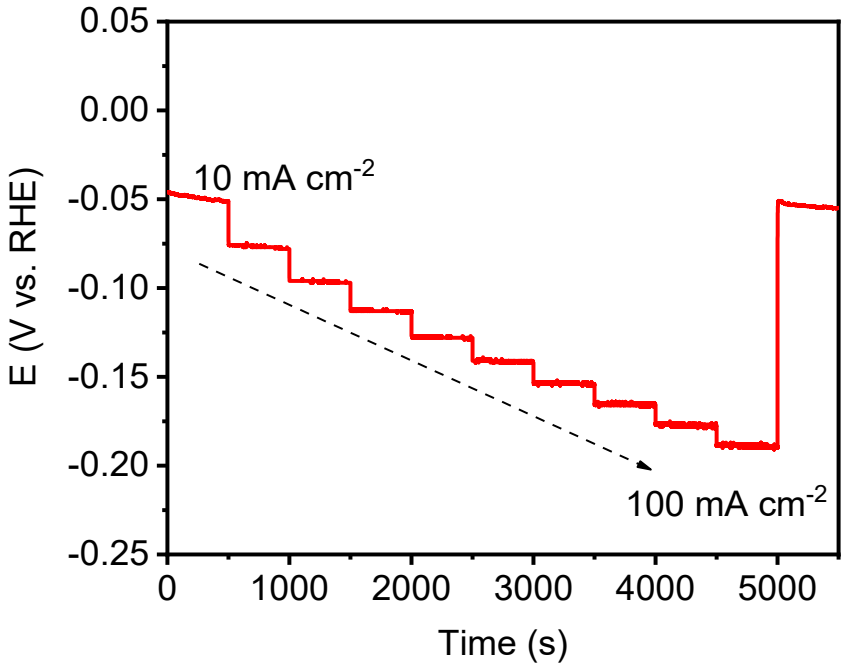

Figure S26. Multi-step chronopotentiometry of the Ru-CoNiS_x/NF catalyst with the current density stepped from 10 to 100 mA cm^{-2} in 1.0 M NaOH.

.

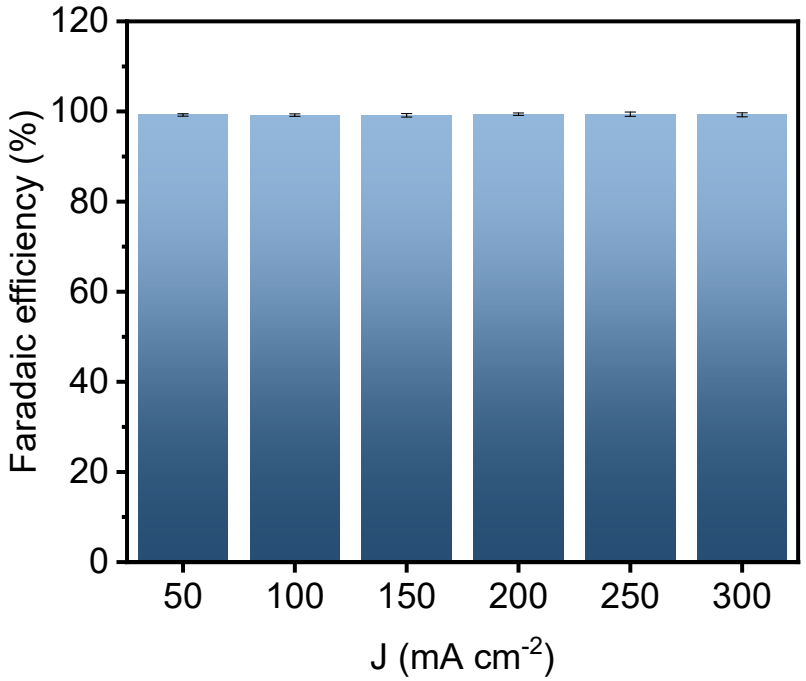

Figure S27. Faradaic efficiency of HER at different current densities.

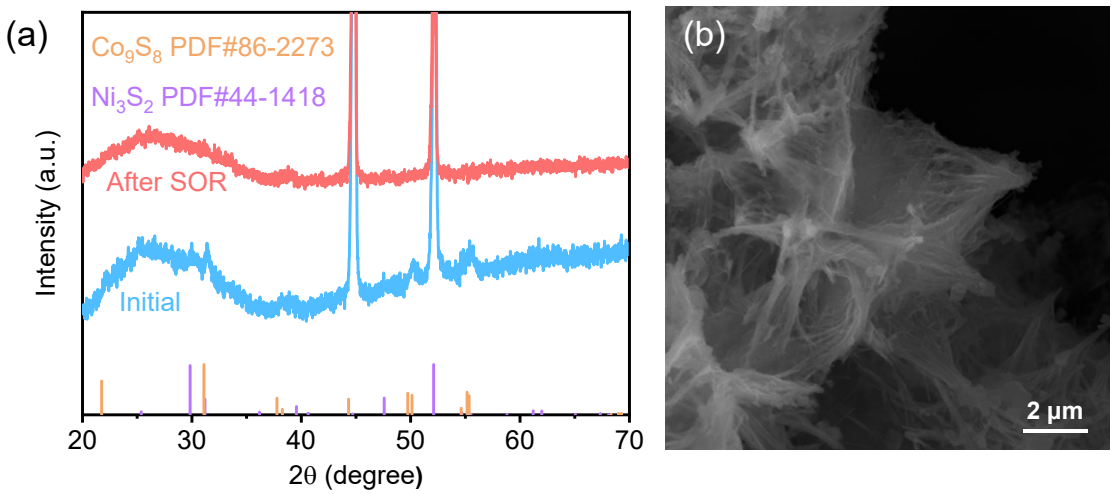

Figure S28 (a) XRD patterns of Ru-CoNiS_x/NF catalyst before and after the SOR stability test. (b) SEM images after the SOR stability test.

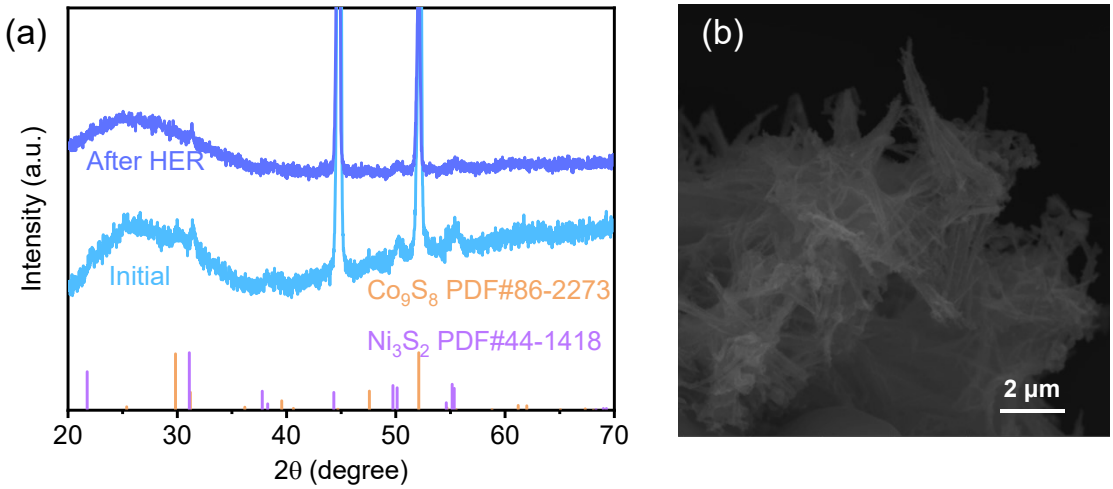

Figure S29. XRD patterns of Ru-CoNiS_x/NF catalyst before and after the HER stability test. (b) SEM images after the HER stability test.

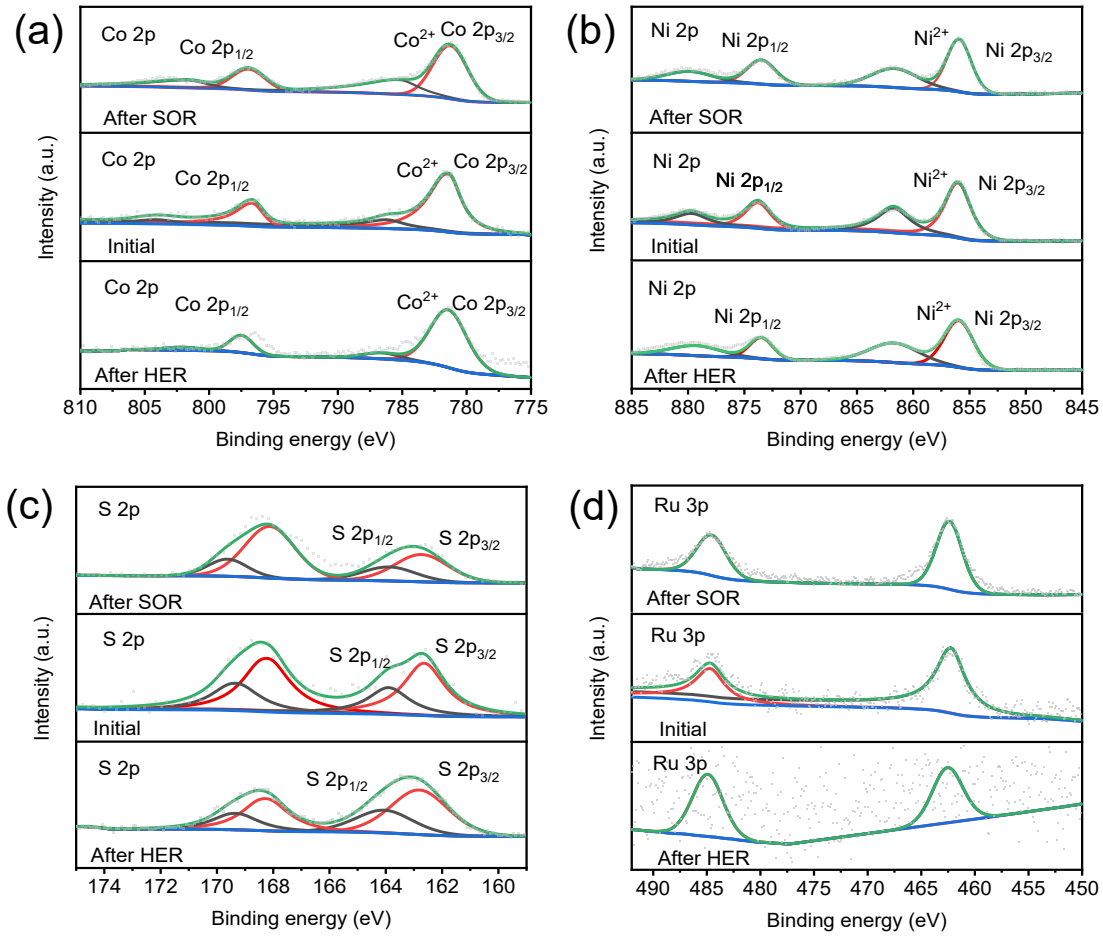

Figure S30. XPS spectrum of the Ru-CoNiS_x/NF catalyst after SOR and HER stability tests.

Table S1 ICP-OES results of Ru-CoNiS_x/NF electrocatalyst.

Element	Co	Ni	Ru
wt%	14.6668	25.5121	9.7162
Relative Metal Atomic At%	0.3192	0.5575	0.1233

Table S2 A comparison of Ru-$CoNiS_x$/NF with reported catalysts in SOR performance.

Catalyst	Electrolyte	Potential (mV vs. RHE) (J=100 mA cm^{-2})	Potential (mV vs. RHE) (J=300 mA cm^{-2})	Ref.
Ru-$CoNiS_x$/NF	**1 M NaOH+1 M Na_2S**	**282**	**358**	**This work**
FeMo-S/Ru	1 M NaOH+2.43 M Na_2S	300	540	[8]
pa-Ru-CoSe	1 M NaOH+1 M Na_2S	273	364	[9]
RuO_2-Co_3O_{4-x}	1 M NaOH+1 M Na_2S	320	400	[10]
Ru-Ni_3S_2/NF	1 M NaOH+1.75 M Na_2S	598	＞800	[11]
VC/Ru@NC	1 M NaOH+2.43 M Na_2S	340	437	[12]
Co_9S_8/CF-V_S	1 M NaOH+1 M Na_2S	387	＞920	[13]
CoS_2@C/ MXene/NF	1 M NaOH+1 M Na_2S	389	648	[14]
Co_3S_4 NWs	1 M NaOH+1 M Na_2S	262	299	[15]

Table S3 Composition of the simulated sulfide-containing wastewater prepared by adding representative coexisting species into 1.0 M NaOH + 1.0 M Na_2S electrolyte.

Chemical	Concentration	
	(mg/L)	(mM)
NaCl	285.5	4.9
KCl	38.0	0.5
$Na_3PO_4 \cdot 12H_2O$	152.0	0.4
Na_2CO_3	625.3	5.9
Na_2SO_4	28.4	0.2
phenol	94.1	1.0

Table S4 A comparison of Ru-$CoNiS_x$/NF with reported catalysts in HER performance.

Catalyst	Tafel slope (mV dec^{-1})	Overpotential (mV)	Ref.
Ru-$CoNiS_x$/NF	**46**	**32**	**This work**
Ru-P-Ni(OH)/NF	52.9	98	[16]
Ni@MoO_2-Ru	91	35.6	[17]
Ru-$Ni(OH)_2$	62.69	51.15	[18]
Ru-NiCoP	86.4	42	[19]
Ru-α-MoC@PC	72	42	[20]
Ru@SC	77.1	88.3	[21]
Ru/TiO_2-A	61	44	[22]
Cu-Ni_3S_2/Co_3S_4	79	50.4	[23]
Fe-Ni_3S_2/NF	95	47	[24]
Ru SAs-Ni_2P	75	57	[25]

Table S5 Metal leaching concentrations in the electrolyte after the SOR stability test.

	Concentration of elements/ppb (ug/L)		
Catalysts	Co	Ni	Ru
Ru-CoNiS_x/NF	31.39	147.05	15.83

Table S6 Metal leaching concentrations in the electrolyte after the HER stability test.

	Concentration of elements/ppb (ug/L)		
Catalysts	Co	Ni	Ru
Ru-CoNiS_x/NF	51.48	108.24	7.29

References

[1] G. Kresse and J. Furthmüller, *Comput. Mater. Sci.*, 1996, **6**, 15-50.

[2] G. Kresse and J. Furthmüller, *Phys. Rev. B*, 1996, **54**, 11169-11186.

[3] J. P. Perdew, K. Burke and M. Ernzerhof, *Phys. Rev. Lett.*, 1996, **77**, 3865-3868.

[4] G. Kresse and D. Joubert, *Phys. Rev. B*, 1999, **59**, 1758-1775.

[5] P. E. Blöchl, *Phys. Rev. B*, 1994, **50**, 17953-17979.

[6] S. Grimme, J. Antony, S. Ehrlich, and H. J. Krieg, *Chem. Phys.*, 2010, **132**, 154104.

[7] J. K. Nørskov, J. Rossmeis, A. Logadottir, L. Lindqvist, J. R. Kitchin, T. Bligaard and H. Jónsson, *J Phys Chem B*, 2004, **46**, 17886-17892.

[8] J. Wang, M. Zhou, R. Fu, J. Ge, W. Yang, X. Hong, C. Sun, X. Liao, Y. Zhao and Z. Wang, *Adv. Funct. Mater.*, 2024, **34**, 2315326.

[9] X. Liu, W. Wang, L. Wan, Y. Hu, C. Xia, L. Cao and B. Dong, *Small*, 2024, **20**, 2406012.

[10] H. Yang, X. Long, F. Liu, J. Zhou, N. Chen, R. Feng, Y. Zhang, X.-Z. Fu, J.-L. Luo and B. Zhao, *Appl. Catal. B: Environ.*, 2025, **366**, 125037.

[11] Q. Zeng, L. Ai, X. Liu, A. Liu and J. Jiang, *Chem. Eng. J.*, 2025, **524**, 167473.

[12] M. Zhou; J. Li, L. Qu, W. Zhang, T. Liu, Y. Liu, F. Wang, Y. Ding, Z. Zhou, Y. Pi, Y. Chen, S. Lee, G. Wang, X. Liao, Y. Zhao, L. Mai, Z. Wang, *Appl. Catal. B: Environ.*, 2026, **383**, 126058.

[13] C. Zhang, Q. Zeng, L. Ai, J. Zhang, X. Wang, A. Liu and J. Jiang, *Chem. Eng. J.*, 2025, **519**, 165491.

[14] L. Zhang, Z. Wang and J. Qiu, *Adv. Mater.*, 2022, **34**, 2109321.

[15] Z. Xiao, C. Lu, J. Wang, Y. Qian, B. Wang, Q. Zhang, A. Tang and H. Yang, *Adv. Funct. Mater.*, 2023, **33**, 2212183.

[16] L. Qian, Y. Zhu, H. Hu, Y. Zheng, Z. Yuan, Y. Dai, T. Zhang, D. Yang, S. Xue and F. Qiu, *J. Colloid Interf. Sci.*, 2024, **669**, 935–943.

[17] Y. Tang, T. Zhou, S. Yu, X. Huang, J. Fu, P. She and Z. Tian, *J. Colloid Interf. Sci.*, 2025, **695**, 137754.

[18] J. Qi, R. Xu, T. Yang, M. Yang, J. Chen, J. Tu, B. Wang, C. Qu, Z. Wang, J. Cao and Y. Yan, *J. Mater. Chem. A,* 2025, **13**, 26555-26563.

[19] Q. T. T. Le, T. T. Nguyen, K. D. Tran, Q. P. Ngo, D. T. Tran, N. H. Kim and J. H. Lee, *Chem. Eng. J.* 2025, **521**, 166378.

[20] F. Sun, Y. Ju, Y. Zhao, C. Yue, N. Liu, H. Hao, Y. Xu, F. Wang, J. Wang and Y. Lu, *Appl. Catal. B: Environ.*, 2026, **382**, 125946.

[21] J. Li, Y. Li, N. Tong, J. Zhang, Q. Tang, N. Wu, G. Liu, H. Chen and X. Liu, *J. Colloid Interf. Sci.*, 2026, **701**, 138796.

[22] E. Li, Y. Shen, Y. Li, Y. Zong, W. Xiao, G. Xu, J. Wang, H. Li, T. Ma, Z. Wu and L. Wang, *Appl. Catal. B: Environ.*, 2026, **382**, 126022.

[23] H. Su, S. Song, S. Li, Y. Gao, L. Ge, W. Song, T. Ma and J. Liu, *Appl. Catal. B: Environ.*, 2021, **293**, 120225.

[24] G. Zhang, Y.-S. Feng, W.-T. Lu, D. He, C.-Y. Wang, Y.-K. Li, X.-Y. Wang and F.-F. Cao, *ACS Catal.*, 2018, **8**, 5431–5441.

[25] K. Wu, K. Sun, S. Liu, W.-C. Cheong, Z. Chen, C. Zhang, Y. Pan, Y. Cheng, Z. Zhuang, X. Wei, Y. Wang, L. Zheng, Q. Zhang, D. Wang, Q. Peng, C. Chen and Y.

Li, *Nano Energy*. 2021, **80**, 105467.